Kinetically Stable Sub-50nm Fluorescent Block Copolymer Nanoparticles via Photomediated RAFT Dispersion Polymerization for Cellular Imaging

Vitalii Tkachenko, Philippe Kunemann, Jean Pierre Malval, Jean-Pierre Malval, Tatiana Petithory, Laurent Pieuchot, Loïc Vidal, Abraham Chemtob

ARTICLE

Kinetically Stable Sub-50nm Fluorescent Block Copolymer Nanoparticles via Photomediated RAFT Dispersion Polymerization for Cellular Imaging

Received 00th January 20xx,
Accepted 00th January 20xx

DOI: 10.1039/x0xx00000x

Vitalii Tkachenko,[a,b] Philippe Kunemann,[a,b] Jean Pierre Malval,[a,b] Tatiana Petithory,[a,b] Laurent Pieuchot,[a,b] Loïc Vidal,[a,b] and Abraham Chemtob*[a,b]

Self-assembled block copolymer nanoparticles (NPs) have emerged as a major potential nanoscale vehicle for fluorescence bioimaging purpose. Crucial to their practical implementation is to prepare with high yields NPs possessing a high kinetic stability to prevent the leakage of fluorophore molecules. Here, we report a photomediated RAFT polymerization-induced self-assembly (PISA) yielding uniform and nanosized poly((oligo(ethylene glycol) acrylate)-*block*-poly(benzyl acrylate) particles (POEGA-*b*-PBzA) with a concentration of 22 w%, over 20 times more than micellization and nanoprecipitation. The spherical diblock copolymer nanoparticles have an average size of 10-50 nm controllable through the degree of polymerization of the stabilizing POEGA block. Subsequent dialysis against water and swelling with Nile red solution lead to highly stable fluorescent NPs able to withstand changes in concentration, ionic strength, pH or temperature. The PBzA/water interfacial tension of 48.6 mN/m hinders the exchange between copolymer chains, resulting in the trapping of NPs in a "kinetically frozen" state responsible for the high stability. A spectroscopic study combining fluorescence and UV-vis absorption agrees with a preferential distribution of fluorophore in the outer POEGEA shell despite its hydrophobic nature. Nile red-doped POEGA-b-PBzA micelles stripped of initiator residue and unimers with high structural stability turn out to be non cytotoxic, and can be used for the optical imaging of cells. Real-time confocal fluorescent microscopy shows a fast cellular uptake using C2C12 cell lines in the matter of minutes, and a preferential localization in the perinuclear region, in particular in the vesicles.

Introduction

Drug delivery and diagnostic imaging are increasingly reliant on nanoscale vehicles.[1] A key reason is their ability to solubilise poorly water-soluble drugs (or contrast agents), a central requirement for improving treatment (or imaging efficacy) and reducing cytotoxic molecule side effects. The portfolio of nanoscale materials used for biomedical or pharmaceutical applications includes liposomes,[2] albumin,[3] inorganic nanoparticles (NPs),[4] and more recently, amphiphilic block copolymer (BC) NPs.[5] The latter represent one of the fastest growing classes of synthetic nanoscopic carriers.[6] The formation of *AB* diblock copolymer NPs proceeds via nanoscale phase separation of a shell-forming solvophilic block *A* acting as steric stabilizer, and a core-forming solvophobic block *B* entrapping generally the drug cargo or the imaging agent. Flory–Huggins interaction parameter (χ_{AB}), solvent quality and block volume fraction are some key parameters governing the self-assembly mechanism.[7] Typically, the active compounds can be incorporated into or onto the NP via ionic interaction, physical trapping, or covalent conjugation. The interest of BC supramolecular aggregates has focused on the targeted delivery of anticancer drugs owing to the ease with which ligands can be attached and the particle diameter tuned.[8] Indeed, size range of several tens of nanometres and surface functionalization have proven to be the most critical factors for maximizing therapeutic efficacy.[9] By contrast, the contribution of BC NPs to bioimaging is still modest. To date, their use is limited to fluorescence optical imaging,[10–19] and to a lesser extent, magnetic resonance imaging.[20] In most studies, the interactions with biological matter have been scarcely addressed.[21,22]

[a] *Université de Haute-Alsace, CNRS, IS2M UMR7361, F-68100 Mulhouse, France. E-mail: abraham.chemtob@uha.fr*
[b] *Université de Strasbourg, France*

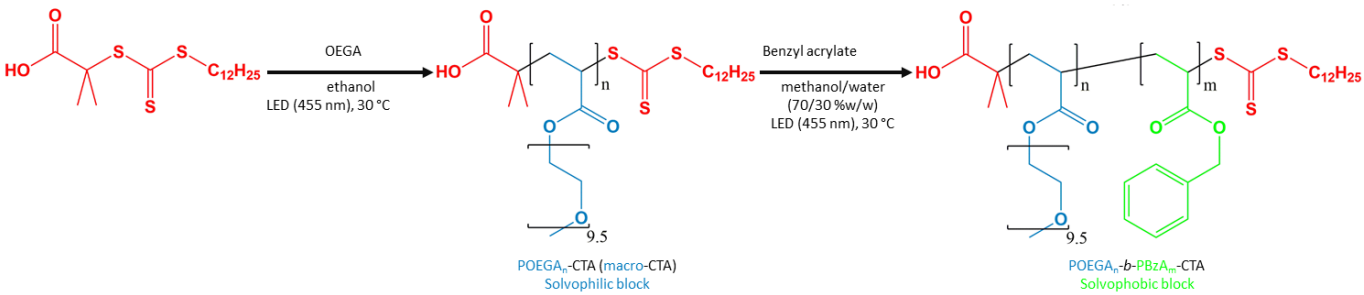

Figure 1. Synthesis of POEGA macro-CTA via photomediated RAFT polymerization in ethanol. Subsequent chain extension via dispersion photo-PISA of benzyl acrylate in a methanol/water mixture.

Fluorescent NPs are currently playing a pivotal role in optical imaging of cells and tissues, but the field is dominated by inorganic NPs, including quantum dots or dye-doped silica NPs.[23] However, fluorescent BC micelles may offer more potential because of their versatility in terms of size, surface properties, composition and range of fluorophores available.[24] For this reason, they can be better customized for the needs of fluorescent imaging where characteristics such as brightness, emission properties, particle diameter, biocompatibility and biodegradability must be balanced depending on the application. BC assemblies do not require additional surfactant due to the steric stabilization provided by the hydrophilic block of the constituting BC.[25] Therefore the NP surface is well-defined, and there are less risks of cytotoxicity caused by surfactant desorption.[26] Despite these advantages, the use of fluorescent BC NPs has been hindered by two problems: the low productivity of the synthetic methods and the limited stability of BC assembly.[27] Dilution, change of pH, temperature or ionic strength can impact the exchange rates between unimers and micelles (kinetic stability) or affect the critical micellar concentration value (thermodynamic stability), causing micelle disassembly and fluorophore cargo release in the biological medium.[28] It is the goal of this research to address these two issues of low productivity and instability of fluorescent BC NPs.

With regard to the first problem, fluorescent BC NPs are generally not produced directly upon polymerization, but from a preformed BC in solution, using either nanoprecipitation or micellization.[25] These methods are not productive since concentration of copolymer NP is less than 1 w%. Since 2008, particular attention has been paid to an original and direct pathway to BC nano-objects referred to as polymerization-induced self-assembly (PISA).[29,30] Among the advantages, there is the possibility to conduct the reaction at high solids content (up to 50 w%)[31–33] and in a single step[34] since copolymer synthesis takes place concomitantly with particle formation. A PISA process starts from a solvophilic block *A* usually prepared through a reversible-deactivation radical polymerization in solution, mainly reversible addition-fragmentation chain-transfer (RAFT) polymerization. This latter soluble polymer acting as steric stabilizer is chain extended with a second monomer to form a second solvophobic block *B*. When this core-forming block reaches a critical degree of polymerization (DP), a spontaneous copolymer self-assembly takes place through a judicious choice of solvent. Very few RAFT-mediated PISA studies deal with the synthesis of fluorescent NPs. Physical trapping of Nile red (NR),[35] pyrene,[36] merocyanine,[37] doxorubicine,[38] or Rhodamine B[39] in PISA-prepared NPs were reported. More recently, covalent conjugation involving (tetraphenylethylene)-azobenzene,[40] cyanine 5[22] and pyrene[41] were described. With only two exception,[22,38] these publications do not discuss the issues linked to cellular interactions of NPs, their spectroscopic properties or kinetic stability.

The present work describes the preparation of fluorescent BC NPs via an initiator-free photomediated RAFT PISA process (**Fig. 1**),[42] in which the initiating radicals are generated by β-cleavage of electronically excited trithiocarbonate control transfer agent (CTA).[43,44] This method obviates the need of initiator or catalyst which could act as toxic residue after synthesis. Our focus has been on NPs based on poly((oligo(ethylene glycol) acrylate)-*block*-poly(benzyl acrylate) (POEGA-b-PBzA) because of two reasons. The pegylated POEGA shell is intended to improve biocompatibility by reducing the immunogenic response (e.g. protein adsorption),[45] while the hydrophobic PBzA core can solubilise and protect the fluorophore. After synthesis, the spherical diblock copolymer NPs have a concentration of 22 w%, which is much higher than the conventional techniques. They are narrowly distributed and show an average size of 10-50 nm controllable through the DP of the solvophilic PEGA block. Sub-50 nm NPs are known to be well-suited to cellular imaging owing to their higher penetration ability. As imaging agent, we have used NR, a lipophilic visible-light fluorophore non covalently bound to the copolymer, encapsulated via a post-synthesis swelling method. Its emission range in 550-650 nm is adapted to optical confocal fluorescent microscopy (CFM) imaging, and its highly hydrophobic nature (predicted logP of 3.6) favours its retention inside the particle. PISA leads to metastable NPs (out of equilibrium) with generally a limited kinetic stability.[46,47] Cross-linking[48] or chemical modification of the core-forming block[49] can be used to improve stability by trapping the micelles into a non-equilibrium state of higher energy barrier, commonly known as “kinetically stable” state or “frozen” state. In this study, the preferred method consists of increasing the interfacial tension between the core-forming block (PBzA) and the continuous phase, by replacing the alcoholic medium (used for the synthesis) by water.[8] The result is a much higher energy cost for the extraction of unimers from micelles, leading to kinetically frozen POEGA-b-PBzA NPs.

This study starts with a comprehensive description of the three-step synthetic route including NP synthesis via PISA, kinetic freezing, and fluorophore encapsulation. The spectroscopic properties of the resulting NR-doped POEGA-b-PBzA NPs. have been extensively investigated using UV-Vis spectroscopy, steady-state and time-resolved fluorescence. Finally, we show that our fluorescent NPs have high potential for cellular optical imaging to study the mechanism and kinetics of cellular uptake.

Experimental section

Materials

Oligo(ethylene glycol) methyl ether acrylate (OEGA) with a number-average molecular weight $\overline{M_n}$ = 480 g mol^{-1} (Sigma-Aldrich, > 96%) was purified by passing through a basic alumina column (Sigma-Aldrich) prior to use. Benzyl acrylate (Alfa Aesar, ≥ 98%) was purified by passing through a basic alumina column (Sigma-Aldrich) prior to use. Ethanol (Fischer Chemical, ≥ 99%), methanol (Fischer Chemical, ≥ 99%), tetrahydrofuran (THF, Sigma-Aldrich, ≥ 99.9%), 2-(dodecylthiocarbonothioylthio)-2-methylpropionic acid (DDMAT, Sigma-Aldrich, 98%), diethyl ether (Sigma-Aldrich, ≥ 99%), NR (TCI, ≥ 98%) were used without purification.

Syntheses

Synthesis of POEGA macro-CTA by photomediated RAFT polymerization of OEGA in solution (ex. POEGA$_{27}$-CTA). OEGA (5.000 g, 13.410 mmol), DDMAT (0.109 g, 0.298 mmol) as CTA and ethanol (10.000 g) were charged into a Schlenk tube equipped with a stirring bar. The mixture was degassed by three freeze–pump–thaw cycles before being placed under nitrogen. The polymerization was conducted inside a LED circular photochemical reactor at 30°C. The photoreactor was constructed by winding a 455 nm LED strip (SMD3528, 60 LED/Meter, Lightingwill, length: 1000 mm) around a quartz cylinder (internal diameter: 60 mm, length: 200 mm). The Schlenk tube was introduced in the axis of the quartz cylinder where it received an irradiance of 0.8 mW·cm^{-2}. Aliquots were regularly withdrawn to determine the conversion by ^{1}H NMR analysis (0.1 mL dissolved in 0.5 mL of D_2O). After 21 h (OEGA conversion of 61%), the polymer was recovered by precipitation into 200 mL of diethyl ether, before being dried under vacuum overnight to give 3.0 g of purified POEGA. The POEGA-CTA was then characterized by SEC in DMF ($\overline{M_n}$ = 11.7× 10^3 g mol^{-1}, $Đ$ = 1.17).

Synthesis of POEGA-b-PBzA NP via photomediated dispersion PISA of benzyl acrylate (ex. POEGA$_{27}$-b-PBzA$_{172}$). POEGA$_{27}$-CTA (0.872 g, 0.067 mmol), benzyl acrylate (1.721 g, 13.317 mmol) and a methanol/water mixture (7.56 g/3.24 g, 70/30 w/w%) were charged into a Schlenk tube equipped with a stirring bar and magnetically stirred during 10 min. The mixture was degassed by three freeze–pump–thaw cycles, then placed under nitrogen. The tube was then exposed during 17 h to the light of a LED circular photoreactor (λ = 455 nm, 0.8 mW cm^{-1}), the temperature being kept at 30°C. A final conversion in benzyl acrylate of 86% was achieved corresponding to a DP of 172. The POEGA-b-PBzA copolymer was then characterized by SEC in DMF ($\overline{M_n}$ = 60.1 × 10^3 g mol^{-1}, $Đ$ = 1.29). In the kinetic study, the mean DP of the PBzA block was varied by adjusting the irradiation time. Aliquots were withdrawn at different reaction times for various analyses (see characterizations section). The syntheses involving POEGA macro-CTA of different lengths were performed by keeping the same monomer/solvent weight ratio 3/10.

Preparation of NR-doped POEGA-b-PBzA NPs via a freezing/encapsulation procedure. POEGA$_{27}$-b-PBzA$_{172}$ NPs dispersed in methanol/water mixture (70/30 w/w%) were dialyzed against a 100 excess of water to replace methanol by water. This dialysis did not cause a colloidal destabilization and led to kinetically stable NPs. The NPs dispersed in water were diluted to reach a polymer concentration of 1 w% (10 mg mL^{-1}). Dye loading was carried out by addition of different volumes of a THF swelling solutions containing different concentrations in NR. Four NR concentrations (0.25, 0.5, 1.0 and 1.5 mM) were studied, and for each, four volume fractions in swelling solutions were added (5, 10, 15 and 20 v%), resulting in 16 samples. Dialysis against water was performed 1 h after addition of the welling solution to remove free fluorophore molecules.

Characterizations

Size exclusion chromatography (SEC). Molecular weights of POEGA-b-PBzA copolymers were determined by SEC at 50°C in DMF containing 0.01 M LiBr. For sample preparation, an aliquot was precipitated in 2 mL of diethyl ether under intense stirring, then the copolymer collected after filtration was dried and dissolved in DMF. Sample solutions with a precise concentration around 1-3 mg mL^{-1} were then prepared and filtered (PTFE membrane; 0.20 µm) before injection. The flow rate was 0.9 mL min^{-1}. The following Agilent 1260 Infinity series setup was used: a G1311A isocratic pump; a G1322A degasser; a G1313A auto-sampler; a G1316A thermostated column compartment equipped with a set of Polymer Laboratories ResiPore columns (nominal particle size: 3 µm; porosity: 2 µm) composed of a guard column (50 × 7.5 mm) and two columns (300 × 7.5 mm); a G1314B variable wavelength detector; a G7800A multidetector suite equipped with a MDS refractive index detector. Relative calibration was performed using a set of EasiVial poly(methyl methacrylate) standards. Agilent SEC software and multi-detector upgrade were used to determine molecular weights and molecular weight dispersities.

Nuclear magnetic resonance (NMR). ^{1}H NMR spectra were recorded in D_2O (POEGA-CTA) or $CDCl_3$ (POEGA-b-PBzA) at 300 MHz on a Varian Mercury spectrometer.

Transmission electron microscopy (TEM). The TEM images of copolymer NPs were obtained with a JEOL ARM-200F instrument working at 200 kV. The images were recorded with camera Gatan, model Orius 1000. 400 mesh gold grids (Agar scientific, ref. AGS162A4) were used. Number-average diameter ($D_n = \sum D_{TEM}/n$ where n is the number of particles) was determined by using a minimum of 200 particles. “Polydispersity index” (PDI) (or “dispersity” as recommended

by IUPAC) was used to describe the breadth of particle size. PDI is defined as D_w/D_n, where $D_w = \sum D_n^4 / \sum D_n^3$. The TEM specimen was subjected to negative staining. Before sample deposition, the TEM grid was irradiated in a glow discharge unit (UV/Ozone ProCleaner *Plus*) for a minimum of 300 s. 70 µL of uranyl acetate (1 w% solution in water) was drawn up into the tip of a 200 µL pipette. 10 µL of the air gap were subsequently drawn up, then a 20 µL of deionized water (acting as washing/mixing agent) followed by another air gap of 10 µL, and finally 10 µL of sample solution (1 w%). The edge of the grid was gripped with a pair of negative pressure tweezers, holding the tweezers so that the grid is angled at approximately 45° facing away from the researcher. The entire content of the pipette tip was ejected across the face of the TEM grid. The excess of stain was removed by touching the torn edge of a piece of filter paper to the edge of the grid. The grid was left to dry over air before analysis.

Measurement of interfacial tensions. Young equation was used to determine PBzA/solvent interfacial tension γ(PBzA/solvent). The solvent is a methanol/water mixture with a weight fraction in methanol ranging from 0 to 70 w%.

$$\gamma(\mathrm{PBzA/solvent}) = \gamma(\mathrm{PBzA/air}) - \gamma(\mathrm{solvent/air})\cos\theta$$

γ(PBzA/air) is the surface free energy between PBzA and air. γ(solvent/air) is the surface tension between solvent and air. θ is the contact angle between PBzA and the solvent. γ(PBzA/air) was obtained with the method of Owens Wendt Rabel Kaelble by contact angle measurements (water and diiodomethane) on a PBzA film using a Goniometer DSA100 (Krüss). γ(solvent/air) was determined with a Tensiometer K12 (Krüss) for a range of methanol/water mixtures. For these measurements, the Wilhelmy method was applied using a platinum plate. Measurements of θ were performed using a PBzA film on top a single drop of solvent (mixture of methanol-water) was applied. To avoid evaporation of methanol, only the first recorded picture of the drop was analysed by drop shape analysis.

UV-Spectroscopy. UV-Vis spectra were obtained using a JascoV730 UV/Vis/NIR spectrophotometer. The selected range of wavelengths was 280-800 nm. This technique was used to determine fluorophore loading (w/w%) in NR-doped POEGA-b-PBzA NPs. Dye loading is the ratio of NR molecules encapsulated to the initial amount of NR used for encapsulation. For this measurement, the sample was diluted 10 times in THF, resulting in a complete dissolution of copolymer and Nile red so that Beer-Lamber Law can be applied to determine dye concentration using a calibration curve.

Steady-state absorption and luminescence spectra. The absorption measurements were carried out with a Perkin Elmer Lambda 2 spectrometer. Steady-state fluorescence spectra in solution were collected from a FluoroMax-4 spectrofluorometer. Emission spectra were spectrally corrected, and fluorescence quantum yields included the correction due to solvent refractive index and were determined relative to Rhodamine 101 in ethanol (Φ_f = 0.92).[50]

Fluorescence lifetime measurements. The fluorescence lifetimes were measured using a Nano LED emitting at 372 nm as an excitation source with a nano LED controller module, Fluorohub from IBH, operating at 1 MHz. The detection was based on an R928P type photomultiplier from Hamamatsu with high sensitivity photon-counting mode. The decays were fitted with the iterative reconvolution method on the basis of the Marquardt/Levenberg algorithm.[51] Such a reconvolution technique allows an overall-time resolution down to 0.2 ns. The quality of the exponential fits was checked using the reduced χ^2 ($\leq$ 1.2).

Cytotoxicity. Mouse C2C12 myoblasts and murine macrophage-like RAW 264.7 cells were used for cytotoxicity assays. Cells were cultured in DMEM (Dulbecco's Modified Eagle's Medium) containing 10 w% fetal bovine serum and 1 w% penicilin/streptomycin, buffered with 20 mM HEPES for RAW cells culture only. Cells were grown into 48 wells plates (1×10^4 cells per well) for 24 h. The medium was replaced by fresh medium containing NPs. Cells were incubated for 6 h and subjected to the MTT (3–(4,5-dimethylthiazol-2-yl)-2,5-diphenyltetrazolium bromide) assay. MTT solution (5.0 mg mL^{-1}; Sigma-Aldrich, Saint Louis, Missouri, USA) was added to each well and incubation at 37°C/5 % CO_2 for 4 h in the dark. Then, the formazan crystals were solubilized in acidified isopropanol and absorbance measurements were performed at 570 nm using a UV-vis spectrophotometer.

Confocal fluorescent microscopy. Particle internalisation was monitored using a spinning disk confocal unit from Yokogawa (CSU W1, Yokogawa Electric Corporation) installed on an inverted Nikon Eclipse Tie2 microscope. Two laser excitation wavelengths were used : 488 nm for CellTracker™ GreenCMFDA and LysoTracker™ Green DND-26, and 555nm for NR trapped in particles. For live acquisition, the spinning disk confocal system was stabilized in temperature (37°C) and CO_2 (5 %) with an Okolab incubation unit.

Results and discussion

I. POEGA-b-PBzA NPs: synthesis, kinetic and colloidal study

I.1 Synthesis of POEGA macro-CTA

For the preparation of POEGA-b-PBzA NPs, a series of POEGA macro-CTAs exhibiting different lengths was first synthesized by photomediated RAFT polymerization in solution. The reaction was conducted without exogenous initiator under blue light (455 nm, 0.8 mW·cm^{-2}) in presence of OEGA and trithiocarbonate DDMAT acting as CTA and photoinitiator (**Fig. 1**). As described in a recent study,[52,53] upon electronic excitation this particular CTA undergoes a cleavage of C-S bond adjacent to the thiocarbonyl chromophor group that yields alkyl and thiyl primary radicals. The kinetic profile for the polymerization of $POEGA_{27}$-CTA is given in **Fig. 2a**. The evolution of OEGA monomer conversion reveals a pseudo first-order kinetic, in line with a constant concentration of propagating species as expected from a reversible-deactivation polymerization. Reaction was stopped after 21 h of irradiation, when a conversion of 61% (see ^{1}H NMR spectra in **Fig. S1** of SI) was achieved leading to an average DP of 27. Due to the low extinction coefficient of the CTA at 455 nm (irradiation

wavelength), β-cleavage was poorly efficient.[53] This results in a limited concentration of active species, leading to sluggish rates compared to a polymerization involving a radical photo(initiator). The narrow molecular weight dispersity ($Đ$ ~ 1.17, **Fig. 2b**) and the linear dependence between monomer conversion and molecular weights (**Fig. 2c**) offer tangible confirmation of controlled mechanism for chains growth. The presence of a shoulder on the GPC trace on the early stage of the reaction may be attributed to a small fraction of low molecular-weight dead chains resulting from termination reactions. Using the same procedure, POEGA macro-CTAs with shorter (DP = 18) and longer chain lengths (DP = 35) were also synthesized (see characterization data in **Table S1** of supporting information SI).

I.2 Synthesis of POEGA-b-PBzA NPs by photomediated RAFT PISA of benzyl acrylate

Kinetic study. $POEGA_{27}$ macro-CTA was then extended with benzyl acrylate in a methanol/water mixture (70/30 w/w%) following the same photomediated RAFT mechanism outlined above (see pictures of the reaction medium taken at different reaction times in **Fig. S2** of SI). As can be seen in **Fig. 3a**, a conversion of 86% was achieved when the reaction was stopped after 17 h of irradiation, leading to a diblock copolymer containing 172 units of benzyl acrylate (NMR spectrum is available in **Fig. S3** in SI). As a result, a copolymer concentration of 22 w% was obtained, a value much higher in comparison with micellization or nanoprecipitation. Conversion and $\ln([M]_0/[M])$ plots as a function of exposure time in Fig. 3a show two intervals with distinct polymerization rates. The underlying reason is the shift of reaction locus. In interval I, the polymerization takes place mainly in solution where low monomer concentration leads to a slow polymerization rate. Interval II begins after nucleation when

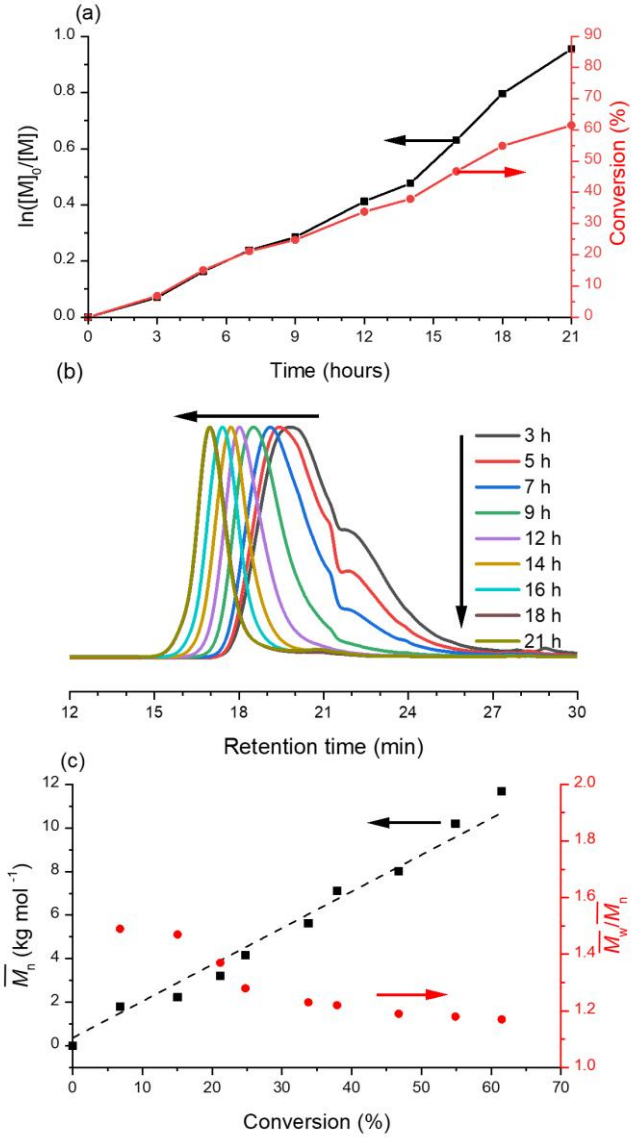

Figure 2. Visible-light photomediated polymerization of OEGA in ethanol for the synthesis of $POEGA_{27}$-CTA. (a) Monomer conversion measured by ^{1}H NMR; (b) SEC chromatograms (RI detector) in DMF; (c) number-average molecular weight ($\overline{M_n}$) and dispersity ($Đ = \overline{M_w}/\overline{M_n}$) as a function of conversion; dashed line: theoretical molecular weight calculated with conversion. Experimental conditions: OEGA:CTA = 45:1 mol; $[OEGA]_0$ = 0.82 M in ethanol, blue LED (0.8 mW cm^{-2}, 30°C).

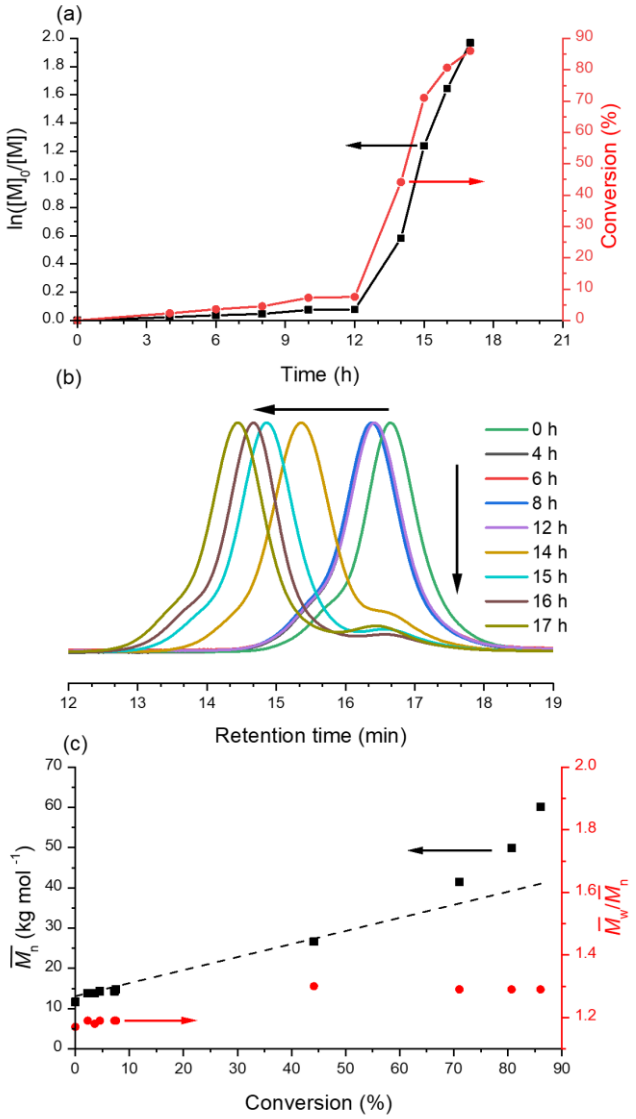

Figure 3. Synthesis of $POEGA_{27}$-*b*-$PBzA_{172}$ via visible-light photomediated polymerization of benzyl acrylate starting from $POEGA_{27}$-CTA. (a) Benzyl acrylate conversion as a function of irradiation (^{1}H NMR data). (b) SEC chromatograms in DMF at 50°C (RI detector) for different irradiation times. (c) Evolution of $\overline{M_n}$ and Đ with monomer conversion; dashed line: theoretical molecular weight. Experimental conditions: BzA:$POEGA_{27}$-CTA= 200:1 mol; $[POEGA_{27}\text{-CTA}]_0$ = 5.21 mM in methanol/water mixture (70/30 w/w%), blue LED (0.8 mW cm^{-2}, 30 °C).

benzyl acrylate-swollen NPs become the main reaction locus. The high local monomer concentration inside the NPs (due to a preferential portioning) causes an acceleration of the polymerization rate.[54,55] The SEC analysis confirms the efficient re-initiation of the RAFT chain-ends and propagation of the chains (**Fig. 3b**). Again, a narrow molecular weight dispersity ($Đ$ ~ 1.29) and a linear relationship between the measured molecular weights and conversions demonstrate that a controlled mechanism is operative (**Fig. 3c**). However, a deviation between the observed and the theoretical molecular weights is apparent at high monomer conversion (> 70%), presumably because of a loss of CTA functionality at longer

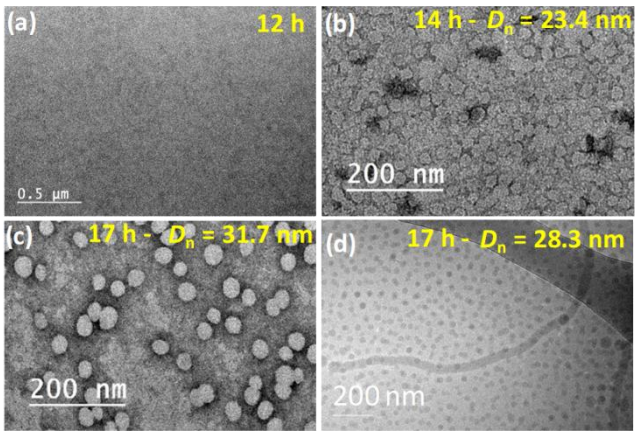

Figure 4. Negative-stained TEM images of $POEGA_{27}$-b-$PBzA_m$ samples taken at different stages of RAFT photomediated PISA of benzyl acrylate: 12 h (a), 14 h (b) and 17 h (c). For comparison, a cryo-TEM image of the same latex after 17 h is also shown (d).

irradiation times.

Colloidal study. Conventional TEM proved unsuitable for imaging the $POEGA_{27}$-b-$PBzA_{172}$ NPs. Due to the low glass transition temperatures of the two polymer blocks (T_g^{POEGA} = -64°C and T_g^{PBzA} = 6°C), the drying required for TEM specimen preparation resulted in coalesced NPs. To preserve the sample's integrity, negative-stain TEM using uranyl acetate was thus performed.[56,57] **Fig. 4** shows some typical images (**a**-**c**) of three negatively stained samples taken at different moments of the synthesis. The minimal time for the formation of NPs was 14 h (image **b**), which is in accordance with the conversion-time curve (Fig. 3a) indicating that interval II (marking the end of nucleation) does not start before 12 h (image **a**). As evidence that the negative staining was successful, the particles in image **b** appear as light areas because of their low electron scattering power relative to the dense surrounding stain, which scatters the electrons more and appears darker. The number-average diameter (D_n) increases progressively with irradiation time: 23.4 nm after 14 h (image **b**), 31.7 nm after 17 h at the end of the reaction (image **c**). The objects exhibit a spherical shape and a narrow particle size dispersity (PDI ≤ 1.04). Since the size strongly influences the biodistribution of NPs and the way of internalization into cells, it is imperative to have well-defined particles with narrow size distributions for bioimaging application. The last sample of composition $POEGA_{27}$-b-$PBzA_{172}$ (obtained at t = 17h) was also analyzed by cryo-TEM, a technique able to image NP in their native state by rapid vitrification (image **d**). The cryo-TEM image features a smaller average diameter of 28.3 nm compared to negative-stain TEM. This result is consistent with our recent findings that negative stain TEM could take into account the thin POEGA shell while this latter is not easily resolved by cryo-TEM.[58] Note the presence of isolated worms in this latter image not visible in the negative-stained TEM image **c**. Conversion of spheres into worms may be promoted by particle swelling with residual monomer since a non-dried sample is analyzed in cryo-TEM. In the presence of non-reacted monomer, the copolymer chains in the NP have a greater mobility that favors morphology change.

Effect of POEGA block length. Table 1 provides the colloidal characteristics of three different copolymer NPs obtained with POEGA macro-CTA of various DPs (18, 27 and 35). The reaction was stopped in order to achieve in all cases a somewhat similar DP of the PBzA block (~180). A shorter stabilizing block ($POEGA_{18}$) causes a drastic increase of particle diameter (D_n = 50.6 nm) due to a higher extent of coalescence events. In contrast, the stronger steric stabilization ability of $POEGA_{35}$ hinders coalescence, leading to a higher number of particles (N_p) and therefore smaller particles (D_n = 13.3 nm). Negative-stained TEM images of $POEGA_{18}$-b-$PBzA_{186}$ and $POEGA_{35}$-b-$PBzA_{180}$ NPs are available in **Fig. S4** of SI

Table 1. Effect of POEGA block length on colloidal data of POEGA-b-PBzA NPs formed by dispersion photo-PISA.

NP	D_n (nm)	PDI	N_p (L^{-1})
$POEGA_{18}$-b-$PBzA_{186}$	50.6 ± 4.6	1.01	2.86×10^{18}
$POEGA_{27}$-b-$PBzA_{172}$	31.7 ± 4.7	1.04	1.22×10^{19}
$POEGA_{35}$-b-$PBzA_{180}$	13.3 ± 2.0	1.04	1.89×10^{20}

D_n – Diameter of NP determined by negative-stained TEM. N_p – Number of NP per liter of dispersion. PDI – particle size dispersity.[59]

II. Preparation of NR-doped kinetically frozen NPs

The procedure to prepare kinetically stable NR-labelled NP is sketched in **Fig. 5**. Starting with a diluted dispersion of $POEGA_{27}$-b-$PBzA_{172}$ NPs (D_n = 31.7 nm, C_p = 10 mg mL^{-1}) in methanol/water mixture, a first dialysis against water was performed to kinetically trap the spherical micelles. The second stage of fluorophore encapsulation consisted of swelling the NP with NR dissolved in a water-miscible organic solvent (THF).[60] The slow removal of the solvent through a second dialysis allows the diffusion of highly hydrophobic NR into the hydrophobic NP core.

II.1 Fluorophore encapsulation

NR encapsulation was optimized upon varying the volume

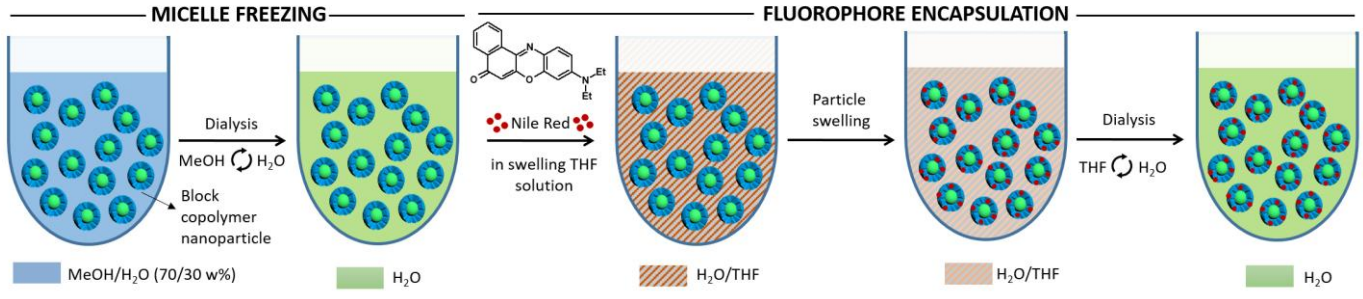

Figure 5. Freezing/encapsulation procedure of NR in $POEGA_{27}$-*b*-$PBzA_{172}$ NPs.

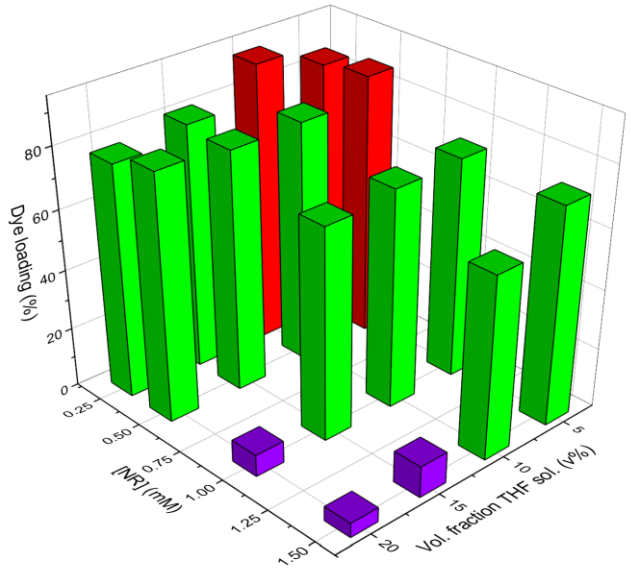

Figure 6. Influence of the volume fraction of THF swelling solution (5-20 v%) and the concentration of NR in the swelling solutions (0.25-1.5 mM) on dye loading in $POEGA_{27}$-b-$PBzA_{172}$ NPs. 3 latexes (red) marked turn out to be highly stable. The other shows severe (violet) or moderate (green) dye precipitation.

fraction of THF swelling solution (5-20 v%) and the concentration of NR in this latter solutions (0.25-1.5 mM). **Fig. 6** illustrates the effect of these two parameters on the relative fraction of incorporated fluorophore (dye loading) for $POEGA_{27}$-b-$PBzA_{172}$. To determine the dye loading, the NR-doped NPs were dissolved in THF, and their absorbance was recorded and compared to a calibration plot. The highest NR concentrations and volume fractions of swelling solutions (violet bars) led to instant dye precipitation or/and particle coalescence, translating the limited loading capacity of the NPs or the destabilization effect of THF. The rest of the samples remained stable after the encapsulation procedure. Nevertheless, gradual fluorophore release took place for a majority of samples after 1 week of storage (green bars), as evidenced by NR precipitation due to its very low water-solubility. Ultimately, only 3 systems (red bars) prepared with the lowest volume fractions of swelling solution (5-10 v%) and NR concentration (0.25 – 0.50 mM) displayed superior and long stability, and were used for the rest of the study. Note that no size variation was reported over more than 6 months of storage. A high fluorophore loading (> 85%) was achieved for this three runs. However, the content of encapsulated dye *ω(NR)* remains limited (0.15 – 0.30 w/w% of copolymer), reflecting a limited NR solubility in the NP. In addition, it would be interest to develop an encapsulation process for concentrated copolymer latexes directly accessible by a PISA process.

II.2 NP kinetic stability

The principle of NP kinetic freezing is to make the exchange of unimers between micelles energetically unfavourable.[61] The method used consists of increasing the interfacial tension between the core-forming block and the continuous phase γ(PBzA/solvent) through a solvent change (from a

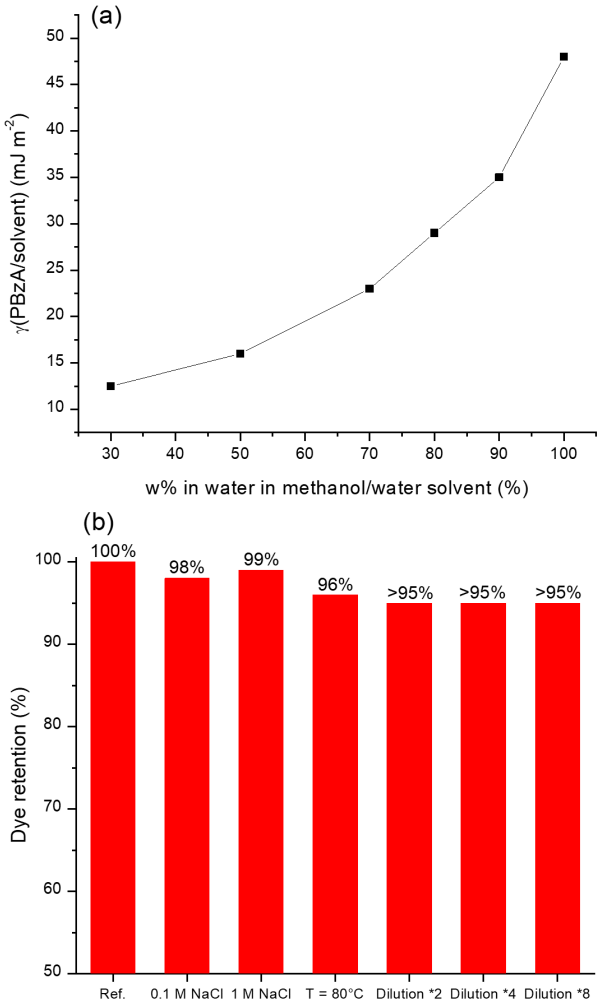

Figure 7. (a) Evolution of γ(PBzA/solvent) as a function of the weight concentration of water in the methanol/water mixture. (b) Retention of NR (%) in $POEGA_{27}$-b-$PBzA_{172}$ NP determined by UV-vis spectroscopy after different treatments. In this series, C_p= 1.6 mg mL^{-1} and [NR] = 2.4 µg L^{-1}.

methanol/water mixture to pure water). **Fig. 7a** shows the evolution γ(PBzA/solvent) depending on the water weight fraction in a methanol/water mixture. As the content of water increases from 30 to 100 w%, the interfacial tension increases progressively from 13.0 to 48.9 mN/m. As reported in the literature, this latter value is assumed to be high enough to displace the micelle/unimer equilibrium of $POEGA_{27}$-b-$PBzA_{172}$ towards micelles, resulting in kinetically frozen NPs.[62] In addition, the use of an aqueous continuous phase in PISA is a well-established method to produce kinetically frozen NPs.[63] To assess experimentally the kinetic stability of $POEGA_{27}$-b-$PBzA_{172}$ NPs (*ω(NR)* = 0.15 w/w% of copolymer), NR retention was investigated after several treatments: dilution in water, addition of NaCl (0.1 and 1 M) and a temperature stress (80 °C, 30 min). As shown in **Fig. 7b**, there is a significant retention of the dye as well as a steady particle size.

III. Spectroscopic properties of dye-doped POEGA-b-PBzA NP

III.1 UV-Vis absorption

The UV-vis spectra of fluorescent $POEGA_{27}$-b-$PBzA_{172}$ NPs at

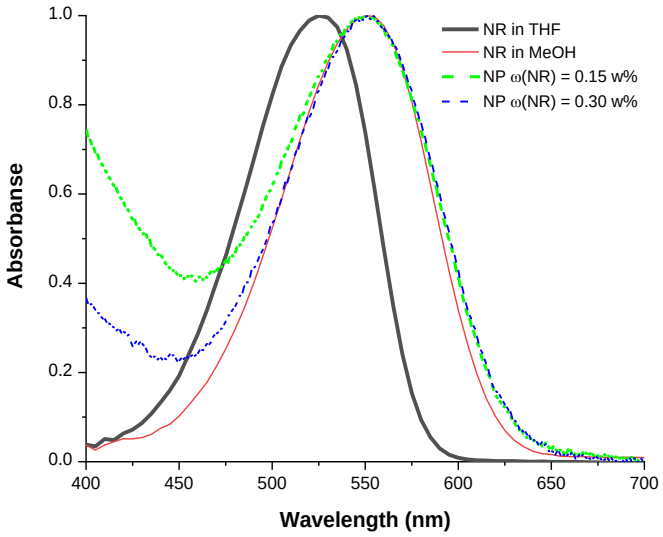

Figure 8. Normalized absorption spectra of NR in solution (THF, methanol) and embedded in $POEGA_{27}$-b-$PBzA_{172}$ NP at two different concentrations: *ω(NR)* = 0.15 and 0.30 w/w% of copolymer.

two dye contents (*ω(NR)* = 0.15 and 0.30 w/w% of copolymer) are shown in **Fig. 8.** To qualitatively estimate the local polarity, the absorption spectra of NR dissolved in THF and methanol were also measured. The dye-labelled NPs exhibit a similar absorption maximum at 550 nm irrespective of the dye content.[64] The value is 40 nm red-shifted in comparison to the spectrum of NR in THF, but matches the NR spectrum in more polar methanol. These data suggest a more polar environment of encapsulated NR as compared to THF. The strong resemblance with the spectrum in methanol is consistent with a preferential localization of NR in the outer POEGA layer despite the high hydrophobicity of the dye. This result is in accordance with other reports on core-shell particles where NR was found to be preferentially solubilized in the outer polar shell.[65,66] Therefore, hydrogen bonding interactions are likely to play an important role in the physical trapping of NR in the NP.

III.2 Steady-state and time-resolved fluorescence

Fig. 9a compares the steady-state fluorescence spectra of NR in solution (using a series of four solvents of different polarities) and in dispersion (using $POEGA_{27}$-b-$PBzA_{172}$ NPs). All the spectroscopic data are summarized in **Table 2**. The normalized fluorescence spectrum of NR is highly sensitive to solvent polarity and undergoes a strong bathochromic shift ($\Delta\lambda$ = 92 nm) when switching from apolar solvent (n-hexane) to highly polar one (acetonitrile). It is worth noting that the emission spectrum in acetonitrile exhibits a red-shifted peak at 618 nm. This latter is close to the one observed at 617 nm in dye-loaded NPs in water. In order to probe the polarity environment of the NR within the NPs, the value of the maximum fluorescence wavenumber of the emitting NPs was reported on the solvatochromic plot of the NR (**Fig. 9b**). Based on the Lippert-Mataga formalism, this latter solvatochromic plot was derived by correlating ν_{fluo}^{max} of the NR in various solvents with the corresponding Lippert-Mataga polarity

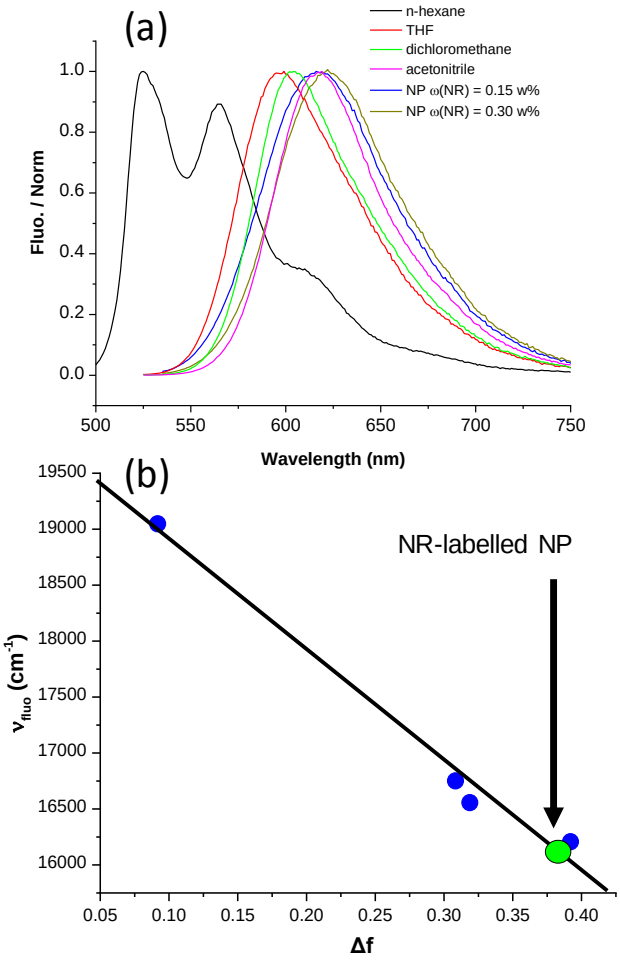

Figure 9. (a) Normalized fluorescence spectra of NR in four different solvents (n-hexane, THF, dichloromethane, acetonitrile) and encapsulated in $POEGA_{27}$-b-$PBzA_{172}$ NP. (b) Lippert-Mataga plot of NR in 4 pure solvents (blue dot) and in $POEGA_{27}$-b-$PBzA_{172}$ (green dot, *ω(NR)* = 0.15 w%). The data are fitted to a straight line (slope) 9700 (R^2 > 0.92).

function (Δf). It can be inferred that the embedded NR in NPs experiences a highly polar environment. This is again in line with a preferential distribution of NR in the outer POEGA shell. Similar conclusions were obtained by investigating the effect gradual addition of water on the fluorescence emission of NR in THF (**Fig. S5** in SI).

Table 2. Fluorescence data of NR in solution and encapsulated in $POEGA_{27}$-b-$PBzA_{172}$ NPs

System	λ_{abs} nm	λ_{fluo} nm	Φ_{fluo}	τ_{fluo} ns	N_{dye}
Solution					
n-Hexane	490	525	0.47	-	-
THF	529	597	0.62	4.3	-
CH_2Cl_2	539	604	0.92	4.4	-
Acetonitrile	527	617	0.75	4.6	-
Dispersion					
ω(NR) = 0.15 w%	550	617	0.55	4.81	52
ω(NR) = 0.30 w%	551	622	0.50	4.44	100

λ_{abs} –maximum absorption of NR, λ_{fluo} – emission maximum of NR, Φ_{fluo} – quantum yield, τ_{fluo} – life-time, N_{dye} – number of NR molecules per NP

As shown in **Table 2**, all the NPs in water are highly luminescent with a fluorescent quantum yield (Φ_{fluo}) higher

than 0.5 for the NPs. However, these latter values are lower than those measured in polar solvents such as dichloromethane or acetonitrile. Such a difference corroborates the occurrence of H-bond interactions between H_2O molecules and excited NR within NPs. Finally, all fluorescence time-dependent decays of NPs are mono-exponential, thus excluding any aggregation effects of

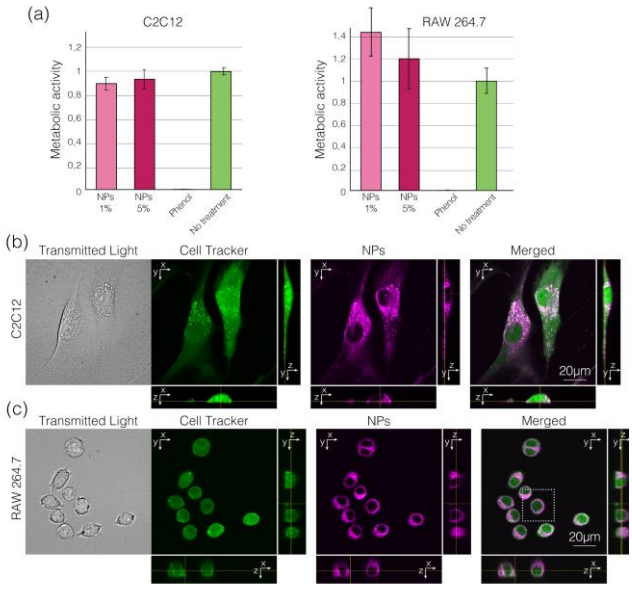

Fig. 10. (a) Cell viability assays (MTT) of NR-loaded $POEGA_{27}$-b-$PBzA_{172}$ NPs (*ω(NR)* = 0.30 w/w% of copolymer) suggesting that NPs are not toxic for either C2C12 or RAW 264.7 cells at C_P = 16 µg mL^{-1} (1%) and 80 µg mL^{-1} (5%). (b) Cellular uptake of NPs in C2C12. (c) Cellular uptake of NPs in RAW 264.7. The cells were labelled with CellTracker (green) in order to visualize the cytosol and incubated with NPs (magenta) for 30 min. The cells were then observed by CFM. Z-series of optical sections were collected for each cell line. A single optical plane (xy) and the corresponding orthogonal views (xz and yz) are shown. NPs accumulate mostly in the perinuclear regions.

encapsulated dyes. NP brightness and photostability were investigated in the SI (**Table S2** and **Fig. S6** of SI).

IV. Cellular interactions

IV.1 Cytoxicity

For bioimaging applications, assessing the non-cytotoxicity and biocompatibility of NPs is an important requirement. Starting with 32 nm $POEGA_{27}$-b-$PBzA_{172}$ NPs including the highest content in NR (*ω(NR)* = 0.30 w/w% of copolymer), in vitro cytotoxicity experiments were performed following a MTT protocol. Two cell lines were used: C2C12 et RAW 264.7. As seen in **Fig. 10a**, after 6 h of incubation at two different polymer concentrations (C_P = 80 and 16 µg mL^{-1}), the cellular metabolic activity of the NP-treated samples was found at the same level as control samples devoid of NPs, irrespective of the cellular type used (results of longer experiment times are given in **Fig. S7** of SI). The highest polymer concentration corresponds to a fluorophore content of 15 nM in water, that is close to the highest concentration used for cellular imaging.[67] Therefore, this experiment shows the absence of toxic effect of NR labelled NPs. The non-toxicity is consistent with the well-established biocompatibility of the individual

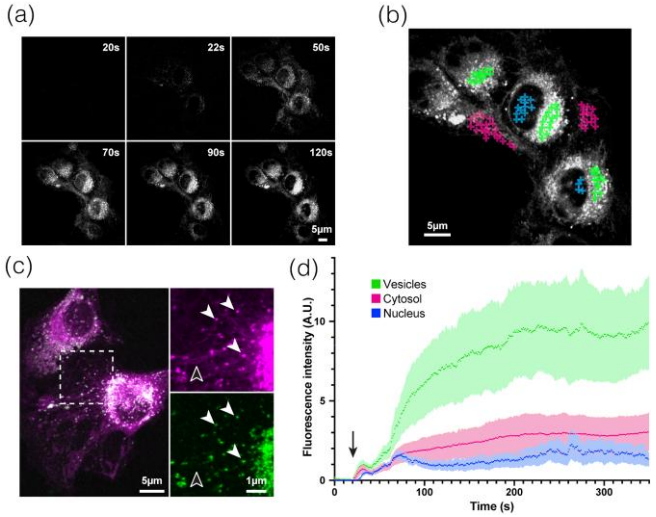

Fig. 11. (a) CFM images of C2C12 cells incubated with NR-labelled $POEGA_{27}$-b-$PBzA_{172}$ NPs (C_P = 80 µg mL^{-1}, *ω(NR)* = 0.30 w/w% of copolymer) 20 s, 22 s, 50 s, 70 s, 90 s, 120 s after the administration. (b) Representative CFM image after 120 s incubation time showing three preferential intracellular NP localizations in perinuclear region (green), plasma membrane (red) and nucleus (blue). (c) Cells labelled with Lysotracker (green) to visualize the lysosomes after incubation with NPs (magenta). The white arrows indicate encapsulation in lysosomes whereas black arrows suggest NP inside cytosol and possibly in endoplasmic reticulum. (d) Kinetics of cellular uptake of NR-encapsulated NPs.

polyacrylate[68] and poly(ethylene oxide)[21] components of the BC. In agreement with our results, the non-cytoxicity of POEGA-b-poly(butyl acrylate) NP was recently reported.[69]

IV.2 Internalization mechanism and kinetics

The internalization of NPs into cells was investigated by CFM. C2C12 cell line was stained with CellTracker Green CMFDA to visualize the entire cells, before subsequent incubation with $POEGA_{27}$-b-$PBzA_{172}$ NPs (C_p = 80 µg mL^{-1}). **Fig 10b** is a CFM image after 30 min indicating that approximately all cells incubated with NPs are fluorescent. Intracellular fluorescence is observed throughout the entire cytosol, with a higher density in perinuclear regions. Despite the relatively low concentration of dye (15 nM in water), the high NP brightness ensures a good signal to noise ratio. To exclude the possibility that the uptake process can be cell line-specific, macrophages (RAW 264.7 cells) were also incubated with NPs and analysed similarly by FCM (**Fig. 10c**). The uptake of NR in the RAW 264.7 cells was found to be very similar to that in C2C12 cells.

Additionally, it is of interest to monitor the rate at which the NPs penetrate across cell membrane. Some representative images of the same C2C12 cells taken at various times after NP injection are given in **Fig. 11a**. Immediately after administration to cells, no fluorescence is measured. A faint fluorescent is measured inside the NPs as early as 22 s after injection as a result of a concentration effect inside the cells. Then, the fluorescent intensity tends to increase, reaches a maximum, and then levels off within 2-3 min. After 2 min, as can be seen in **Fig 11b**, the NPs are not distributed homogeneously, but are preferentially localized in the perinuclear region (green) as seen previously, and to a minor extent, in the plasma membrane (red) and the nucleus (blue).

In the region around the nucleus, the appearance of discrete patches is consistent with their inclusion in cytoplasmic vesicles such as endosomes and lysosomes. **Fig 11c** is an image of C2C12 cells stained with a Lysotracker (green spots, white arrows) selective lysosomal tracking. A significant colocalization was observed with NR-labelled NPs (magenta spots, white arrows) that supports NPs accumulation in lysosomes. There is also a diffuse NR fluorescence in the cytosol and also in other membrane structures which look like endoplasmic reticulum (black arrow). Finally, the difference of fluorescence intensity was used to quantify the subcellular distribution of internalized NR in the three main different intracellular regions: vesicles, cytosol and nucleus. **Fig. 11d** is a real-time uptake kinetics of the NPs based on the average fluorescence intensity in these three regions. Irrespective of the intracellular area, the fluorescence intensity increases rapidly and reaches a plateau within 2-3 min. Our data support the very limited ability of NPs to enter the nucleus, consistently with results obtained with variant poly(oligoethylene glycol methacrylate)- poly(styrene-co-vinylbenzaldehyde) NPs of similar size.[70] In addition, This result supports the NP kinetic stability since release of dye molecules would cause a decreased intensity due to severe fluorescence in in water.[71] The most striking feature remains the extremely fast internalization, taking place in the seconds after administration. The diameter of the NP used in this study is about 30 nm. Such size range has been poorly described in studies on internalization mechanism.[72] Nanostructures with typical between 50-200 nm are generally subjected to endocytosis.[68] Smaller NPs are assumed to penetrate the cell membranes through a different passive pathway such as pore formation and diffusion.[73] In agreement with the fact uptake kinetics, such translocation mechanism may occur at a much faster rate than a conventional endocytotic pathway.[21]

Conclusions

Well-defined spherical diblock copolymer NPs based on POEGA-b-PBzA were prepared via an initiator-free RAFT photomediated PISA process. Sub-50 nm particles were encapsulated with NR fluorophore through a conventional swelling procedure. A low saturation threshold of NR in NP was found (~ 0.30 w/w% of polymer). To ensure superior kinetic stability and maximize fluorophore retention, the NPs were converted into kinetically frozen micelles through solvent exchange from water/methanol to pure water. This non-equilibrium state enables to prepare kinetically stable NPs. Accordingly, the resulting NR-labelled NPs dispersed in water were hardly disturbed by dilution, temperature stress and change of pH and ionic force. Spectroscopic study supported a single site localization of the dye in the POEGEA polar shell despite the presence of apolar PBzA core. Encapsulated NR showed minimal aggregation, high fluorescence quantum yield and photostability. Cytotoxicity investigations revealed the biocompatibility of NPs, and preliminary cell uptake assay demonstrated fast cellular internalization. We believe that such surfactant-free NPs with adjustable size and high kinetic stability are suitable candidate to study how nanoparticles interact with cells.

Conflicts of interest

There are no conflicts to declare.

Acknowledgements

This research was funded by the Ministry of Higher Education and Research in France ("Ministère de l'Enseignement Supérieur et de la Recherche", MESR) for granting a PhD fellowship to Vitalii Tkachenko

Notes and references

1 Y. Malam, M. Loizidou and A. M. Seifalian, *Trends Pharmacol. Sci.*, 2009, **30**, 592–599.
2 T. M. Allen and P. R. Cullis, *Adv. Drug Deliv. Rev.*, 2013, **65**, 36–48.
3 B. Elsadek and F. Kratz, *J. Controlled Release*, 2012, **157**, 4–28.
4 R. Liang, M. Wei, D. G. Evans and X. Duan, *Chem. Commun.*, 2014, **50**, 14071–14081.
5 A. M. Bodratti and P. Alexandridis, *J. Funct. Biomater.*, 2018, **9**, 11.
6 C. L. Waite and C. M. Roth, *Crit. Rev. Biomed. Eng.*, , DOI:10.1615/CritRevBiomedEng.v40.i1.20.
7 J. C. Brendel and F. H. Schacher, *Chem. – Asian J.*, 2018, **13**, 230–239.
8 Y. Zhang, W. Song, J. Geng, U. Chitgupi, H. Unsal, J. Federizon, J. Rzayev, D. K. Sukumaran, P. Alexandridis and J. F. Lovell, *Nat. Commun.*, 2016, **7**, 11649.
9 K. Kataoka, A. Harada and Y. Nagasaki, *Adv. Drug Deliv. Rev.*, 2012, **64**, 37–48.
10 M. P. Robin, S. A. M. Osborne, Z. Pikramenou, J. E. Raymond and R. K. O'Reilly, *Macromolecules*, 2016, **49**, 653–662.
11 S. M. Parke, S. Tanaka, H. Yu, E. Hupf, M. J. Ferguson, Y. Zhou, K. Naka and E. Rivard, *Macromolecules*, 2019, **52**, 7477–7488.
12 T. Bai, D. Shao, J. Chen, Y. Li, B. B. Xu and J. Kong, *J. Colloid Interface Sci.*, 2019, **552**, 439–447.
13 Y. Zhao, Y. Wu, B. Xue, X. Jin and X. Zhu, *Polym. Chem.*, 2018, **10**, 77–85.
14 T. Cao, P. Munk, C. Ramireddy, Z. Tuzar and S. E. Webber, *Macromolecules*, 1991, **24**, 6300–6305.
15 J. Hu, L. Dai and S. Liu, *Macromolecules*, 2011, **44**, 4699–4710.
16 G. Wu, S.-C. Chen, C.-L. Liu and Y.-Z. Wang, *Acs Nano*, 2015, **9**, 4649–4659.
17 A. Wagh, S. Y. Qian and B. Law, *Bioconjug. Chem.*, 2012, **23**, 981–992.
18 G. Sun, M. Y. Berezin, J. Fan, H. Lee, J. Ma, K. Zhang, K. L. Wooley and S. Achilefu, *Nanoscale*, 2010, **2**, 548–558.
19 W.-C. Wu, C.-Y. Chen, Y. Tian, S.-H. Jang, Y. Hong, Y. Liu, R. Hu, B. Z. Tang, Y.-T. Lee, C.-T. Chen, W.-C. Chen and A. K.-Y. Jen, *Adv. Funct. Mater.*, 2010, **20**, 1413–1423.
20 W. Zhao, H. T. Ta, C. Zhang and A. K. Whittaker, *Biomacromolecules*, 2017, **18**, 1145–1156.
21 M. J. Barthel, A. C. Rinkenauer, M. Wagner, U. Mansfeld, S. Hoeppener, J. A. Czaplewska, M. Gottschaldt, A. Träger, F. H. Schacher and U. S. Schubert, *Biomacromolecules*, 2014, **15**, 2426–2439.
22 M. N. Vu, H. G. Kelly, A. K. Wheatley, S. Peng, E. H. Pilkington, N. A. Veldhuis, T. P. Davis, S. J. Kent and N. P. Truong, *Small*, 2020, **16**, 2002861.
23 O. S. Wolfbeis, *Chem. Soc. Rev.*, 2015, **44**, 4743–4768.
24 M. P. Robin and R. K. O'Reilly, *Polym. Int.*, 2015, **64**, 174–182.
25 A. Reisch and A. S. Klymchenko, *Small*, 2016, **12**, 1968–1992.
26 S. K. Sahoo, J. Panyam, S. Prabha and V. Labhasetwar, *J. Controlled Release*, 2002, **82**, 105–114.
27 S. C. Owen, D. P. Y. Chan and M. S. Shoichet, *Nano Today*, 2012, **7**, 53–65.

28 A. Richter, C. Olbrich, M. Krause, J. Hoffmann and T. Kissel, *Eur. J. Pharm. Biopharm.*, 2010, **75**, 80–89.
29 F. D'Agosto, J. Rieger and M. Lansalot, *Angew. Chem. Int. Ed.*, 2020, **59**, 8368–8392.
30 N. J. W. Penfold, J. Yeow, C. Boyer and S. P. Armes, *ACS Macro Lett.*, 2019, **8**, 1029–1054.
31 J. Wang, Z. Wu, G. Wang and K. Matyjaszewski, *Macromol. Rapid Commun.*, 2018, 1800332.
32 B. Karagoz, L. Esser, H. T. Duong, J. S. Basuki, C. Boyer and T. P. Davis, *Polym. Chem.*, 2013, **5**, 350–355.
33 J. Rieger, *Macromol. Rapid Commun.*, 2015, **36**, 1458–1471.
34 L. D. Blackman, K. E. B. Doncom, M. I. Gibson and R. K. O'Reilly, *Polym. Chem.*, 2017, **8**, 2860–2871.
35 B. Karagoz, C. Boyer and T. P. Davis, *Macromol. Rapid Commun.*, 2014, **35**, 417–421.
36 A. Bagheri, C. Boyer and M. Lim, *Macromol. Rapid Commun.*, 2019, **40**, 1800510.
37 C.-Q. Huang, Y. Wang, C.-Y. Hong and C.-Y. Pan, *Macromol. Rapid Commun.*, 2011, **32**, 1174–1179.
38 L. Zhang, L. Xie, S. Xu, R. P. Kuchel, Y. Dai, K. Jung and C. Boyer, *Biomacromolecules*, 2020, **21**, 3887–3897.
39 X.-F. Xu, C.-Y. Pan, W.-J. Zhang and C.-Y. Hong, *Macromolecules*, 2019, **52**, 1965–1975.
40 Y. Zhou, Z. Wang, Y. Wang, L. Li, N. Zhou, Y. Cai, Z. Zhang and X. Zhu, *Polym. Chem.*, 2020, **11**, 5619–5629.
41 J. Y. Rho, G. M. Scheutz, S. Häkkinen, J. B. Garrison, Q. Song, J. Yang, R. Richardson, S. Perrier and B. S. Sumerlin, *Polym. Chem.*, 2021, **12**, 3947–3952.
42 V. Tkachenko, C. Matei Ghimbeu, C. Vaulot, L. Vidal, J. Poly and A. Chemtob, *Polym. Chem.*, 2019, **10**, 2316–2326.
43 J. Yeow and C. Boyer, *Adv. Sci.*, 2017, **4**, 1700137.
44 J. Yeow, O. R. Sugita and C. Boyer, *ACS Macro Lett.*, 2016, **5**, 558–564.
45 S. Naahidi, M. Jafari, F. Edalat, K. Raymond, A. Khademhosseini and P. Chen, *J. Controlled Release*, 2013, **166**, 182–194.
46 S. L. Canning, G. N. Smith and S. P. Armes, *Macromolecules*, 2016, **49**, 1985–2001.
47 Y. Zhang, Z. Wang, K. Matyjaszewski and J. Pietrasik, *Eur. Polym. J.*, 2019, **110**, 49–55.
48 X. Shuai, T. Merdan, A. K. Schaper, F. Xi and T. Kissel, *Bioconjug. Chem.*, 2004, **15**, 441–448.
49 M. G. Carstens, P. H. J. L. F. de Jong, C. F. van Nostrum, J. Kemmink, R. Verrijk, L. G. J. de Leede, D. J. A. Crommelin and W. E. Hennink, *Eur. J. Pharm. Biopharm.*, 2008, **68**, 596–606.
50 B. Valeur, *Mol. Fluoresc.*, 2001, 399.
51 K. A. Zachariasse, *Nachrichten Aus Chem. Tech. Lab.*, 1985, **33**, 896–896.
52 B. Cabannes-Boué, Q. Yang, J. Lalevée, F. Morlet-Savary and J. Poly, *Polym. Chem.*, 2017, **8**, 1760–1770.
53 J. Xu, S. Shanmugam, N. A. Corrigan and C. Boyer, in *Controlled Radical Polymerization: Mechanisms*, American Chemical Society, 2015, vol. 1187, pp. 247–267.
54 J. Tan, J. He, X. Li, Q. Xu, C. Huang, D. Liu and L. Zhang, *Polym. Chem.*, 2017, **8**, 6853–6864.
55 J. He, Q. Xu, J. Tan and L. Zhang, *Macromol. Rapid Commun.*, 2018, 1800296.
56 C. J. Ferguson, G. T. Russell and R. G. Gilbert, *Polymer*, 2002, **43**, 6371–6382.
57 C. Gaillard, G. Fuchs, C. J. G. Plummer and P. A. Stadelmann, *Micron*, 2007, **38**, 522–535.
58 V. Tkachenko, L. Vidal, L. Josien, M. Schmutz, J. Poly and A. Chemtob, *Polymers*, 2020, **12**, 1656.
59 A. Nematollahzadeh, M. J. Abdekhodaie and A. Shojaei, *J. Appl. Polym. Sci.*, 2012, **125**, 189–199.
60 T. Behnke, C. Würth, E.-M. Laux, K. Hoffmann and U. Resch-Genger, *Dyes Pigments*, 2012, **94**, 247–257.
61 T. Nicolai, O. Colombani and C. Chassenieux, *Soft Matter*, 2010, **6**, 3111–3118.
62 M. Jacquin, P. Muller, H. Cottet, R. Crooks and O. Théodoly, *Langmuir*, 2007, **23**, 9939–9948.
63 V. J. Cunningham, A. M. Alswieleh, K. L. Thompson, M. Williams, G. J. Leggett, S. P. Armes and O. M. Musa, *Macromolecules*, 2014, **47**, 5613–5623.
64 J. Swain and A. K. Mishra, *Photochem. Photobiol. Sci.*, 2016, **15**, 1400–1407.
65 E. Fleige, B. Ziem, M. Grabolle, R. Haag and U. Resch-Genger, *Macromolecules*, 2012, **45**, 9452–9459.
66 S. Bhatia, A. Mohr, D. Mathur, V. S. Parmar, R. Haag and A. K. Prasad, *Biomacromolecules*, 2011, **12**, 3487–3498.
67 K. Trofymchuk, A. Reisch, I. Shulov, Y. Mély and A. S. Klymchenko, *Nanoscale*, 2014, **6**, 12934–12942.
68 A. Vollrath, A. Schallon, C. Pietsch, S. Schubert, T. Nomoto, Y. Matsumoto, K. Kataoka and U. S. Schubert, *Soft Matter*, 2012, **9**, 99–108.
69 C. Chen, F. Richter, C. Guerrero-Sanchez, A. Traeger, U. S. Schubert, A. Feng and S. H. Thang, *ACS Macro Lett.*, 2020, **9**, 260–265.
70 E. Hinde, K. Thammasiraphop, H. T. T. Duong, J. Yeow, B. Karagoz, C. Boyer, J. J. Gooding and K. Gaus, *Nat. Nanotechnol.*, 2017, **12**, 81–89.
71 S. Snipstad, S. Westrøm, Y. Mørch, M. Afadzi, A. K. Åslund and C. de Lange Davies, *Cancer Nanotechnol.*, 2014, **5**, 8.
72 S. Behzadi, V. Serpooshan, W. Tao, M. A. Hamaly, M. Y. Alkawareek, E. C. Dreaden, D. Brown, A. M. Alkilany, O. C. Farokhzad and M. Mahmoudi, *Chem. Soc. Rev.*, 2017, **46**, 4218–4244.
73 H. Ding, W. Tian and Y. Ma, *ACS Nano*, 2012, **6**, 1230–1238.